Title: Asymmetric hysteresis response of midlatitude storm tracks to CO_2 removal

Author list: Jaeyoung Hwang[1], Seok-Woo Son[1*], Chaim I. Garfinkel[2], Tim Woollings[3], Hyunsuk Yoon[1], Soon-Il An[4,5], Sang-Wook Yeh[6], Seung-Ki Min[5,7], Jong-Seong Kug[5], and Jongsoo Shin[8]

Affiliations: [1]School of Earth and Environmental Sciences, Seoul National University, Seoul, South of Korea.

[2]Fredy and Nadine Herrmann Institute of Earth Sciences, The Hebrew University of Jerusalem, Edmond J. Safra Campus, Givat Ram, Jerusalem, Israel

[3]Atmospheric, Oceanic and Planetary Physics, University of Oxford, Oxford, United Kingdom

[4]Department of Atmospheric Sciences/Irreversible Climate Change Research Center, Yonsei University, Seoul, South Korea

[5]Division of Environmental Science and Engineering, Pohang University of Science and Technology (POSTECH), Pohang, South Korea

[6]Department of Marine Sciences and Convergence Technology, Hanyang University, ERICA, Ansan, South Korea

[7]Institute for Convergence Research and Education in Advanced Technology, Yonsei University, Seoul, South Korea

[8]Woods Hole Oceanographic Institution, Woods Hole, Massachusetts, United States

[*]Corresponding Author: Seok-Woo Son (email: seokwooson@snu.ac.kr).

Abstract

In a warming climate, storm tracks are projected to intensify on their poleward side. Here we use large-ensemble CO_2 ramp-up and -down simulations to show that these changes are not reversed when CO_2 concentrations are reduced. If CO_2 is removed from the atmosphere following CO_2 increase, the North Atlantic storm track keeps strengthening until the middle of the CO_2 removal, while the recovery of the North Pacific storm track during ramp-down is stronger than its shift during ramp-up. In contrast, the Southern Hemisphere storm track weakens during ramp-down at a rate much faster than its strengthening in the warming period. Compared to the present climate, the Northern Hemisphere storm track becomes stronger and the Southern Hemisphere storm track becomes weaker at the end of CO_2 removal. These hemispherically-asymmetric storm track responses are attributable to the weakened Atlantic meridional overturning circulation and the delayed cooling of the Southern Ocean.

Keywords: Storm track, Carbon Dioxide Removal

Main text

The midlatitude storm tracks, where extratropical cyclones are commonly found, are fundamental features of the climate system. Arising from baroclinic instability, the Northern Hemisphere (NH) storm tracks are centered over the North Pacific (NP) and North Atlantic (NA), while the Southern Hemisphere (SH) storm track is hemispheric. Storm tracks effectively transport heat, moisture, and momentum poleward, contributing to the global energy balance[1,2,3]. They also have a profound impact on the day-to-day variability of local weather. The mobile cyclones within storm tracks explain more than 50% of the midlatitude precipitation[4]. In particular, explosive and/or consecutive cyclones are responsible for extreme events such as heavy precipitation, storm surges, and wind gusts, leading to the devastating socio-economic impacts[5,6].

Given their importance in local weather and global hydroclimate, storm track changes caused by human activity have been of great interest[7]. The projected changes in storm tracks due to increasing greenhouse gases show regional and seasonal dependence in state-of-the-art climate models[8,9,10,11,12,13]. During the NH winter, a weakened storm track is anticipated on the equatorward side of the NP storm track, whereas an eastward extension is projected to occur on the northeastern flank of the NA storm track[8,10,11,13]. During the summer, an overall weakening of the NH storm tracks is found[8,11,13]. Conversely, the SH storm track show a systematic poleward intensification in a warming climate especially in austral summer[8,11,12,13].

To reduce future climate risk, both carbon dioxide removal (CDR) and the reduction of carbon dioxide emissions have been suggested[14,15]. Their possible impacts on the climate system have then been investigated by conducting climate model experiments[16,17]. An example is the CDR Model Intercomparison Project (CDRMIP)[18] as a part of the 6th Coupled Model Intercomparison Project (CMIP6)[19]. This experiment and other similar experiments have shown that the climate response to CO_2 removal is not simple, raising the possibility of irreversible climate change[16,20,21,22,23,24,25,26].

However, previous studies have primarily focused on the changes in basic climate elements such as temperature and precipitation[20,21,22,23,26]. Little emphasis has been placed on midlatitude weather and climate systems.

By conducting a large ensemble CDR experiment (CDR-LE; Methods), here we show that midlatitude storm tracks exhibit a hysteresis response to a symmetric CO_2 increase-and-decrease scenario, the hysteresis being defined as a difference between the two time periods when CO_2 concentrations are identical in transient ramp-up and –down simulations. They respond non-monotonically in the NH but monotonically in the SH to CO_2 removal. Their possible causes are discussed by considering sea surface temperature (SST) changes.

Hemispherically-asymmetric storm track changes

A time evolution of global-mean surface air temperature (orange) in the CDR-LE is shown in Fig. 1a. Both the ensemble-mean response (solid) and the ensemble spread (shading) are presented. During CO_2 increasing period, referred to as ramp-up (RU), surface air temperature increases linearly. At the time of quadrupled CO_2 (year 2140), it becomes ~5 K warmer than the present-day (PD) condition (gray dashed line). This warming trend is reversed into a cooling trend as CO_2 concentrations in the atmosphere are reduced during ramp-down (RD). However, the cooling trend is slightly weaker than the warming trend, resulting in a warmer surface air temperature at the end of RD (year 2280) compared to the PD state[24,27]. In the stabilization period when CO_2 concentrations are maintained to the PD level, surface air temperature is still above the PD level by ~1K for approximately 40 years, until it slowly decreases. It does not return to the PD state even at the end of the stabilization period, exemplifying the hysteresis response of climate system to CO_2 concentration change[26,28,29].

With increasing CO_2 concentrations, the latitude of the NH storm track, where a maximum zonal-mean eddy kinetic energy (EKE) is found (Methods), is projected to move poleward (Fig. 1b)

[8,10,13]. It gradually shifts equatorward when CO_2 concentrations are reduced, and eventually returns to the initial latitude at the end of RD. The SH storm track latitude shows a qualitatively similar evolution to the NH storm track latitude (Fig. 1d). It shifts poleward during RU and is then maintained at a fixed latitude for ~20 years when CO_2 concentrations start to decrease. The poleward-shifted storm track moves equatorward in early RD and is fully recovered in the stabilization period. These results indicate that the position of the storm track responds almost linearly to a changing CO_2 pathway.

Such a symmetrical change is not found in storm track intensity (Figs. 1c,e). The NH storm track intensity gradually increases during RU, emerging from internal variability within ~40 years (see the timing when red line and blue shading start to diverge in Fig. 1c)[30]. This storm track strengthening is not reversed during RD. Instead of weakening, the NH storm track intensifies during the first half of RD, even faster than during RU, reaching a peak at the year 2200 of ~12% stronger intensity than the PD state. Afterwards, it rapidly weakens with a large ensemble spread, but its intensity at the end of RD is still stronger than the PD state. The storm track weakening continues after CO_2 removal (until ~2320), although not significantly different from the PD state. As in the NH, the SH storm track intensifies during RU, becoming ~14% stronger than the PD state at the year 2140 (Fig. 1e). However, it sharply weakens during RD at a rate faster than its strengthening. At the end of RD, the storm track intensity is ~3% weaker than the PD state. Although storm track intensity slowly increases toward its initial state in the stabilization period, it is not fully recovered.

It is noteworthy that the internal variability of storm track intensity, quantified by the model ensemble spread (red shading in Figs. 1c,e), is nearly constant during RU. This is consistent with previous studies reporting that internal climate variability does not change much in a warming climate[31]. However, the internal variability of the NH storm track intensity becomes larger in mid and late RD compared to RU (Fig. 1c). It indicates that the internal climate variability can be sensitive to CO_2 pathway, potentially manifested as uncertainty in the timing of the storm track recovery.

106 This asymmetric behavior in the NH storm track manifests differently in the NP and NA storm
107 tracks. This is diagnosed by the maximum eddy kinetic energy at each longitude (Fig. 2a). The
108 asymmetric NH storm track intensity change to symmetric CO_2 pathway is mostly due to the NA storm
109 track centered at the Greenwich meridian. It sharply contrasts to the NP storm track centered at the
110 date line, which shows a slow weakening followed by a rather fast recovery and overshoot. This zonal
111 asymmetry is not evident in the SH (Fig. 2b).

112 The differences in storm track intensity between the peak CO_2 period (2121-2160) and early
113 RU (2001-2040), and between late RD (2241-2280) and the peak period are further analyzed in Figs.
114 2c,d. As a reference, the PD state, which resembles the observations[8,10,13], is superimposed in each plot
115 (contours). With increasing CO_2 concentrations, the NP storm track is weakened with a slight
116 intensification on its northern flank (Fig. 2c). The NA storm track in contrast shows a northeastward
117 intensification. In the SH, a poleward intensification of the storm track is found at all longitudes during
118 RU. Such changes are commonly found in the CMIP6 models (Supplementary Fig. 1). Storm track
119 intensity changes during RD are largely opposed to those during RU, but not exactly (Fig. 2d). The
120 NH storm track in late RD becomes stronger than that in early RU over both the NP and NA (Fig. 2e).
121 It contrasts to the SH storm track that is weaker in late RD than in early RU. Such hemispherically-
122 contrasting storm track intensity changes are strongest in the winter hemisphere (Supplementary Fig.
123 2), and not sensitive to the definition of the storm track (Supplementary Fig. 3).

124 Individual cyclones are also tracked in the lower troposphere (Fig. 3; Methods). In a warming
125 climate, a decrease in NP cyclones and a northeastward expansion of NA cyclones are projected to
126 occur, with an overall decrease in cyclones passing over the continent (Supplementary Fig. 4a)[8,11,12,32].
127 In the SH, a robust poleward shift in cyclone track is simulated. A similar response is also found for
128 intense cyclones that are more localized over the oceans (Supplementary Fig. 4b). These changes are
129 reversed during RD (Supplementary Figs. 4c,d). However, both NP and NA cyclones are still more
130 frequent during late RD compared to early RU (Fig. 3a). This is in contrast to SH cyclones which

become less frequent in late RD. These changes are qualitatively similar to Eulerian storm track changes (Fig. 2e), especially for intense cyclones (Fig. 3b).

Role of the ocean

Although the dominant mechanism(s) of storm track changes in future climate still remains to be determined[9,12], it has been widely accepted that its changes are largely associated with the baroclinicity[13]. The time evolution of vertically integrated mean available potential energy, which is roughly proportional to the square of Eady growth rate[33,34,35], shows a qualitatively similar result (Supplementary Fig. 5). Regional storm track changes (Figs. 2c-e) are also similar to mid-tropospheric zonal wind change (Supplementary Fig. 6), as anticipated from a close relationship between westerly jets and storm tracks in midlatitudes[10,13]. These results suggest that changes in storm track intensity can be understood by considering drivers of the background baroclinicity such as the SST gradient[36].

The SST changes under the time-varying CO_2 pathway are not homogeneous in space (Figs. 4a-c). During RU, NA SST shows localized cooling to the south of Greenland, known as a warming hole (Fig. 4a)[37]. This warming hole, possibly caused by a reduced influx of warm water from low latitudes linked to the Atlantic Meridional Overturning Circulation (AMOC)[27,37,38,39], results in an enhanced meridional SST gradient over the NA, strengthening the westerly jet and storm track. During RD, NA SST becomes colder than the CO_2 peak period (Fig. 4b). The net result is colder NA SST during late RD compared to early RU (Fig. 4c), explaining the hysteresis response of the NA storm track intensity. The close relationship among the NA storm track, jet, and SST gradient also appears in their temporal evolutions (Fig. 4d).

A skewed-parabolic change of the NA SST gradient is largely due to the delayed response of the AMOC (Fig. 4d), highlighting a potential role of the AMOC in NA climate change[40,41]. During RU, AMOC gets weaker due to enhanced surface freshwater and heat fluxes[42,43,44]. The strength of the

AMOC keeps decreasing until the middle of RD due to a reduced horizontal salt advection[45], and rapidly recovers afterward because of an increased salt advection feedback driven by the subtropic-to-subpolar salinity gradient and oceanic stratification changes[27]. The prolonged weakening of the AMOC maintains an anomalously strong SST gradient in the NA which drives a strong baroclinicity and an intense storm track.

The NP storm track intensity shows an opposite evolution to the NA storm track intensity, although the overall change is smaller (Fig. 4e). Its change is again closely related to the SST gradient change in the region. During RU, SST warms faster in the midlatitude than in the subtropics (Figs. 4a and Supplementary Fig. 7a), reducing the local SST gradient (blue in Fig. 4e). This latitudinally-varying SST change is partly attributable to ocean heat redistribution in the NP[46]. In response to the SST gradient change, the intensities of the NP storm track and jet weaken with time[47]. During RD, a faster SST cooling in the midlatitude than in the subtropics strengthens the local SST gradient (Fig. 4c), leading to stronger storm track and jet intensities in the region (see Supplementary Discussion 1).

However, the NP storm track intensity change cannot be explained by the local SST gradient change alone. While the NP SST gradient is weaker during late RD than early RU, the NP storm track is stronger (compare early RU and late RD in Fig. 4e). Moreover, the NP SST gradient does not show a local maximum around the year 2260, when the storm track intensity reaches its maximum. These suggest that the NP storm track intensity is determined not only by the local SST gradient but also by other factors. One possible factor is the tropical Pacific SST. The tropical eastern Pacific SST warms and cools throughout RU and RD, respectively, with the cooling being weaker than the warming. The net result is the El Niño-like SST anomaly at the end of RD compared to the initial state (Fig. 4c). Given the fact that the NP storm track strengthens on the equatorward side of their climatological locations during El Niño condition[1,48], a slow cooling of the tropical eastern Pacific SST (purple in Fig. 4e) may be partly responsible for the strengthening and southeastward extension of the NP storm track during RD (see Supplementary Discussion 1 and Supplementary Fig. 8)[1,47,48].

In the SH, the poleward intensifying jet and storm track during RU align with a stronger warming in the midlatitude than in the Southern Ocean[49,50], although a declined Antarctic sea ice tends to weaken or shift the jet equatorward[51,52]. A rather slow SST change over the Southern Ocean is likely due to an equatorward energy redistribution from the increased highlatitude ocean heat uptakes[53] (purple in Fig. 4f), with the meridional overturning circulation change in the ocean and surface westerly change in the atmosphere[54]. During RD, the delayed cooling is projected to occur in the Southern Ocean (Fig. 4b), partly due to its large heat capacity[24,55,56,]. The reduced SST gradient (blue in Fig. 4f), which is smaller than the one during RU, explains the weakened SH storm track (green) and jet intensities (brown) during late RD compared to early RU.

Discussion

Here, we investigate the reversibility or hysteresis of midlatitude storm tracks in response to CO_2 removal. By conducting large ensemble CO_2 removal experiments, we show that the projected storm track intensity changes may be asymmetric in response to a symmetric CO_2 increase-and-decrease pathway with a noticeable hemispherical asymmetry and basin dependency. The NA storm track changes do not reverse for several decades after CO_2 levels begin to decline. Distinct from the NA, the NP and SH storm tracks show an immediate and rapid recovery during CO_2 removal period, although the final state at the end of CO_2 removal is different from the initial state in both cases. Such changes are closely related to ocean hysteresis such as the weakened AMOC, the slow cooling of equatorial eastern Pacific SST, and the delayed cooling of the Southern Ocean during CO_2 removal period. The larger internal variability of the NH storm track intensity during late CO_2 removal period than during CO_2 increase period is also closely related with the uncertainty in ocean response to CO_2 removal, especially the AMOC (Supplementary Fig. 9). Although the ocean response to CO_2 removal

may have a model dependency, the multi-model mean response from CDRMIP shows similar results, supporting the present study (Supplementary Discussion 2 and Supplementary Figs. 10-12).

The hysteresis response of midlatitude storm tracks to CO_2 removal is summarized in Fig. 5. Both the NA and NP storm track intensity changes take anticlockwise trajectories with CO_2 concentration changes indicating stronger storm tracks in ramp-up than in ramp-down at identical CO_2 concentrations (Figs. 5a,b), although their trends in a warming period are opposite. In contrast, the SH storm track intensity change follows a clockwise trajectory, with a weaker intensity at the end of CO_2 removal. Such hemispheric difference is also found in the reversibility. While both the NA and NP storm track intensities eventually return to the present-day state during the stabilization period, the SH storm track intensity is not fully reversed at the end of the stabilization period. This suggests that the SH storm track takes much longer time than the NH storm track to return to the present-day state.

This result indicates that future projections of day-to-day weather variability cannot be scaled by the atmospheric CO_2 concentration or global-mean surface air temperature changes. The changes in midlatitude weather systems have often been linearly related with the global-mean surface air temperature changes[57], especially when assessing climate risks[58]. However, a linear relationship in present and warm climate may not hold when global-mean surface temperature decreases through climate intervention[59] (Fig. 1a; see also Supplementary Fig. 13).

Although the projected storm track changes are relatively modest in time-varying CO_2 pathways when compared to the climatological states, their surface impacts are significant enough to warrant attention[60,61]. For instance, cyclone-related surface wind extremes become more frequent in southern North America and Europe during late CO_2 removal period compared to early CO_2 increasing period, but less frequent over North America (Supplementary Fig. 14), which align with storm track changes. In the SH, cyclone-related surface wind extremes are projected to decrease by ~40% during late CO_2 removal period compared to early CO_2 increasing period. This suggests that basin-dependent

and hemispherically-asymmetric storm track changes in response to CO_2 removal may have significant impacts on extreme weather. Lastly, our finding shows that substantial time is required to reach an equilibrium state after CO_2 removal. It implies that climate policy and monitoring efforts concerning climate intervention should necessarily be long-term in nature.

Acknowledgements

Model simulation and data transfer were supported by the National Supercomputing Center with supercomputing resources including technical support (KSC-2021-CHA-0030), the National Center for Meteorological Supercomputer of the Korea Meteorological Administration (KMA), and by the Korea Research Environment Open NETwork (KREONET), respectively. We acknowledge the World Climate Research Programme, which, through its Working Group on Coupled Modelling, coordinated and promoted CMIP6. We appreciate the climate modeling groups for producing and making available their model output, the Earth System Grid Federation (ESGF) for archiving the data and providing access (https://esgf-node.llnl.gov/projects/cmip6/), and the multiple funding agencies who support CMIP6 and ESGF. S.-W. Son was supported by the National Research Foundation of Korea (NRF) grant funded by the Korea government (2018R1A5A1024958 and 2023R1A2C3005607).

Author Contributions Statement

J. Hwang conducted analysis, illustrated the figures, and wrote the manuscript. S.-W. Son conceptualized the overall research idea and wrote the manuscript. C. Garfinkel and T. Woollings improved the interpretation of the results and wrote the manuscript. H. Yoon assisted in the computation of Lagrangian storm tracks. All of the authors discussed the results and reviewed the manuscript.

Competing Interests Statement

The authors declare no competing interests.

253 **Figure Legends / Captions**

254 **Fig. 1 | Global surface air temperature and hemispheric storm track changes during CO_2**
255 **pathway. a**, Time series of the CO_2 concentration (black) and annual mean global surface air
256 temperature anomaly with respect to PD (orange). The solid line and shading indicate ensemble mean
257 of the temperature and a standard deviation of its spread, respectively. **b-e,** Time series of the
258 differences of latitudinal storm track position (**b,d**) and intensity (**c,e**), where the maximum of the
259 zonal-mean storm track activity is observed in Northern Hemisphere (**b,c**) and Southern Hemisphere
260 (**d,e**), during ramp-up (RU), ramp-down (RD), and stabilization (ST) simulations. The storm track is
261 represented by the vertically averaged 2-8 day bandpass filtered EKE. The solid line denotes time-
262 mean and ensemble-mean storm track characteristics in present day (blue; PD) and in the experiments
263 (red), respectively. Shadings display the interdecadal variability in the PD period (light blue) and a
264 standard deviation of the experiment ensemble spread (light red), respectively. The surface temperature
265 is 11-year running averaged.

266

267 **Fig. 2 | Spatial distribution of storm track changes during CO_2 pathway.** Hovmöller diagrams of
268 ensemble-averaged annual-mean storm track intensity change in the Northern Hemisphere (**a**) and
269 Southern Hemisphere (**b**), and its spatio-temporal change during CO_2 increasing (**c**) and decreasing
270 period (**d**), and its hysteresis response (**e**). In panels **a,b**, the intensity is averaged within 3-grid points
271 in latitude surrounding the maximum zonal-mean storm track activity in the model. Shades denoted
272 the differences compared to PD simulation. In panels **c-e**, the CO_2 increasing period is defined by the
273 difference between early RU (2001-2040) and CO_2 peak (2121-2160) periods. The decreasing period
274 is defined as the difference between CO_2 peak (2121-2160) and late RD (2241-2280) periods. The
275 shading in **e** depicts the difference of storm track intensity between the periods of late RD and early
276 RU. The values which are statistically significant at the 95% confidence level (two-tailed t-test) are
277 dotted. Three regions showing large EKE hysteresis have been framed with black boxes in **e** (North

Atlantic: 40ºW-40ºE, 40º-60ºN; North Pacific: 150º-230ºE, 30º-50ºN, Southern Hemisphere: 30º-60ºS). As a reference, the climatology of the storm track (contour; 10 m^2 s^{-2} interval) in the PD simulation is superimposed.

Fig. 3 | Hysteresis response of cyclone track density. Hysteresis response of ensemble-averaged annual-mean cyclone track density (tracks/month) of total (**a**) and intense cyclones (**b**). Black contours indicate the climatological cyclone track density of total (2 tracks/month; **a**) and intense cyclones (0.5 tracks/month; **b**) in the PD simulation. Dotted regions indicate statistically significant differences at the 95% confidence level (two-tailed t-test). The low-latitude regions (less than 20 degree) are masked.

Fig. 4 | Spatial distribution of SST and regional storm track changes during CO_2 pathway. a-c, Projected change of ensemble-averaged annual-mean sea surface temperature (SST; K) during CO_2 increasing (**a**) and decreasing period (**b**), and its hysteresis response (**c**) as in Figs. 2c-e. The values which are statistically significant at the 95% confidence level (two-tailed t-test) are dotted. **d-f,** The time series of storm track intensity (m^2 s^{-2}; green lines; boxed regions in Fig. 2**e**), SSTy (K; blue lines; boxed regions in **c**), and U500 (m s^{-1}; brown lines; boxed regions in Supplementary Fig. 6) over North Atlantic (**d**), North Pacific (**e**), and Southern Hemisphere (**f**). The SSTy is defined as high-latitude minus and low-latitude SST differences (North Atlantic: 60ºW-0º, 35º-65ºN; North Pacific: 150º-230ºE, 20º-50ºN; and Southern Hemisphere: 30º-60ºS). The negative SSTy indicates the enhanced SST gradient in the region. The purple lines in **d-f** show the strength of AMOC (Sv), SST changes over the Niño3.4 region (170°-120°W, 5°N-5°S) in winter, and upward (into atmosphere) surface turbulent heat flux (THF; W m^{-2}) around Southern Ocean (50°-70°S), respectively. Dark and light colors in **d-f** denote the ensemble mean and a standard deviation of ensemble spreads, respectively. The strength of AMOC is obtained by averaging the annual-mean Atlantic meridional ocean stream function from 35°N to

45°N at 1000 m depth, where the climatological maximum strength is found in the PD simulation. The time series are smoothed by the 11-year running mean.

Fig. 5 | Regional storm track changes as a function of CO_2 concentrations. Changes of EKEs (m^2 s^{-2}; boxed regions in Fig. 2**e**) in North Atlantic (**a**), North Pacific (**b**), and Southern Hemisphere (**c**) as a function of CO_2 concentrations. The ramp-up (RU; violet), ramp-down (RD; green), and stabilization (ST; yellow) periods are denoted with different colors. Individual ensembles and their mean are denoted in light and dark dots, respectively.

References

1. Chang, E.K., Lee, S. & Swanson, K.L. Storm track dynamics. *Journal of climate* **15**, 2163-2183 (2002).
2. Wu, Y., Ting, M., Seager, R., Huang, H.-P. & Cane, M.A. Changes in storm tracks and energy transports in a warmer climate simulated by the GFDL CM2. 1 model. *Climate dynamics* **37**, 53-72 (2011).
3. Caballero, R. & Hanley, J. Midlatitude eddies, storm-track diffusivity, and poleward moisture transport in warm climates. *Journal of the atmospheric sciences* **69**, 3237-3250 (2012).
4. Hawcroft, M., Shaffrey, L., Hodges, K. & Dacre, H. How much Northern Hemisphere precipitation is associated with extratropical cyclones? *Geophysical Research Letters* **39** (2012).
5. Pfahl, S. & Wernli, H. Quantifying the relevance of cyclones for precipitation extremes. *Journal of Climate* **25**, 6770-6780 (2012).
6. Lehmann, J. & Coumou, D. The influence of mid-latitude storm tracks on hot, cold, dry and wet extremes. *Scientific reports* **5**, 1-9 (2015).
7. Shaw, T.A. Mechanisms of future predicted changes in the zonal mean mid-latitude circulation. *Current Climate Change Reports* **5**, 345-357 (2019).
8. Chang, E.K., Guo, Y. & Xia, X. CMIP5 multimodel ensemble projection of storm track change under global warming. *Journal of Geophysical Research: Atmospheres* **117** (2012).
9. Shaw, T. *et al.* Storm track processes and the opposing influences of climate change. *Nature Geoscience* **9**, 656-664 (2016).
10. Harvey, B., Cook, P., Shaffrey, L. & Schiemann, R. The response of the northern hemisphere storm tracks and jet streams to climate change in the CMIP3, CMIP5, and CMIP6 climate models. *Journal of Geophysical Research: Atmospheres* **125**, e2020JD032701 (2020).
11. Priestley, M.D. & Catto, J.L. Future changes in the extratropical storm tracks and cyclone intensity, wind speed, and structure. *Weather and Climate Dynamics* **3**, 337-360 (2022).
12. Tamarin-Brodsky, T. & Kaspi, Y. Enhanced poleward propagation of storms under climate change. *Nature geoscience* **10**, 908-913 (2017).
13. Lehmann, J., Coumou, D., Frieler, K., Eliseev, A.V. & Levermann, A. Future changes in extratropical storm tracks and baroclinicity under climate change. *Environmental Research Letters* **9**, 084002 (2014).
14. Vaughan, N.E. & Lenton, T.M. A review of climate geoengineering proposals. *Climatic change* **109**, 745-790 (2011).
15. Rogelj, J. *et al.* Mitigation pathways compatible with 1.5°C in the context of sustainable development. In: *Global warming of 1.5 °C. An IPCC Special Report on the Impacts of Global warming of 1.5 °C above Pre-Industrial Levels and Related Global Greenhouse Gas Emission Pathways, in the Context of Strengthening the Global Response to the Threat of Climate Change, Sustainable Development, and Efforts to Eradicate Poverty* (eds Masson-Delmotte, V. et

al.) https://www.ipcc.ch/site/assets/uploads/sites/2/2019/05/SR15_Chapter2_Low_Res.pdf (2018).

16. Frölicher, T.L. & Joos, F. Reversible and irreversible impacts of greenhouse gas emissions in multi-century projections with the NCAR global coupled carbon cycle-climate model. *Climate dynamics* **35**, 1439-1459 (2010).

17. Wu, P., Ridley, J., Pardaens, A., Levine, R. & Lowe, J. The reversibility of CO 2 induced climate change. *Climate Dynamics* **45**, 745-754 (2015).

18. Keller, D.P. *et al.* The carbon dioxide removal model intercomparison project (CDRMIP): rationale and experimental protocol for CMIP6. *Geoscientific Model Development* **11**, 1133-1160 (2018).

19. Eyring, V. *et al.* Overview of the Coupled Model Intercomparison Project Phase 6 (CMIP6) experimental design and organization. *Geoscientific Model Development* **9**, 1937-1958 (2016).

20. Armour, K., Eisenman, I., Blanchard-Wrigglesworth, E., McCusker, K. & Bitz, C. The reversibility of sea ice loss in a state-of-the-art climate model. *Geophysical Research Letters* **38** (2011).

21. Boucher, O. *et al.* Reversibility in an Earth System model in response to CO2 concentration changes. *Environmental Research Letters* **7**, 024013 (2012).

22. Chadwick, R., Wu, P., Good, P. & Andrews, T. Asymmetries in tropical rainfall and circulation patterns in idealised CO2 removal experiments. *Climate dynamics* **40**, 295-316 (2013).

23. Mathesius, S., Hofmann, M., Caldeira, K. & Schellnhuber, H.J. Long-term response of oceans to CO2 removal from the atmosphere. *Nature Climate Change* **5**, 1107-1113 (2015).

24. Kug, J.-S. *et al.* Hysteresis of the intertropical convergence zone to CO2 forcing. *Nature Climate Change* **12**, 47-53 (2022).

25. Song, S.-Y. *et al.* Asymmetrical response of summer rainfall in East Asia to CO2 forcing. *Science Bulletin* **67**, 213-222 (2022).

26. Kim, S.-K. *et al.* Widespread irreversible changes in surface temperature and precipitation in response to CO2 forcing. *Nature Climate Change* **12**, 834-840 (2022).

27. An, S.I. *et al.* Global cooling hiatus driven by an AMOC overshoot in a carbon dioxide removal scenario. *Earth's Future* **9**, e2021EF002165 (2021).

28. Zickfeld, K., MacDougall, A.H. & Matthews, H.D. On the proportionality between global temperature change and cumulative CO2 emissions during periods of net negative CO2 emissions. *Environmental Research Letters* **11**, 055006 (2016).

29. Lee, J.-Y. *et al.* Future global climate: scenario-based projections and near-term information, (IPCC, 2021).

30. Hawkins, E. & Sutton, R. Time of emergence of climate signals. *Geophysical Research Letters* **39** (2012).

31. Thompson, D.W., Barnes, E.A., Deser, C., Foust, W.E. & Phillips, A.S. Quantifying the role of internal climate variability in future climate trends. *Journal of Climate* **28**, 6443-6456 (2015).

32. Zappa, G., Shaffrey, L.C., Hodges, K.I., Sansom, P.G. & Stephenson, D.B. A multimodel assessment of future projections of North Atlantic and European extratropical cyclones in the CMIP5 climate models. *Journal of Climate* **26**, 5846-5862 (2013).

33. O'Gorman, P.A. & Schneider, T. Energy of midlatitude transient eddies in idealized simulations of changed climates. *Journal of climate* **21**, 5797-5806 (2008).

34. Mbengue, C. & Schneider, T. Storm-track shifts under climate change: Toward a mechanistic understanding using baroclinic mean available potential energy. *Journal of the Atmospheric Sciences* **74**, 93-110 (2017).

35. Gertler, C.G., O'Gorman, P.A. & Pfahl, S. Moist available potential energy of the mean state of the atmosphere and the thermodynamic potential for warm conveyor belts and convection. *Weather and Climate Dynamics* **4**, 361-379 (2023).

36. Nakamura, H., Sampe, T., Tanimoto, Y. & Shimpo, A. Observed associations among storm tracks, jet streams and midlatitude oceanic fronts. *Earth's Climate: The Ocean–Atmosphere Interaction, Geophys. Monogr* **147**, 329-345 (2004).

37. Keil, P. *et al.* Multiple drivers of the North Atlantic warming hole. *Nature Climate Change* **10**, 667-671 (2020).

38. Zhang, R. *et al.* A review of the role of the Atlantic meridional overturning circulation in Atlantic multidecadal variability and associated climate impacts. *Reviews of Geophysics* **57**, 316-375 (2019).

39. Chemke, R., Zanna, L. & Polvani, L.M. Identifying a human signal in the North Atlantic warming hole. *Nature communications* **11**, 1540 (2020).

40. Woollings, T., Gregory, J.M., Pinto, J.G., Reyers, M. & Brayshaw, D.J. Response of the North Atlantic storm track to climate change shaped by ocean–atmosphere coupling. *Nature Geoscience* **5**, 313-317 (2012).

41. Bellomo, K., Angeloni, M., Corti, S. & von Hardenberg, J. Future climate change shaped by inter-model differences in Atlantic meridional overturning circulation response. *Nature Communications* **12**, 3659 (2021).

42. Gregory, J. *et al.* A model intercomparison of changes in the Atlantic thermohaline circulation in response to increasing atmospheric CO2 concentration. *Geophysical Research Letters* **32** (2005).

43. Kim, H. & An, S.-I. On the subarctic North Atlantic cooling due to global warming. *Theoretical and applied climatology* **114**, 9-19 (2013).

44. Bakker, P. *et al.* Fate of the Atlantic Meridional Overturning Circulation: Strong decline under continued warming and Greenland melting. *Geophysical Research Letters* **43**, 12,252-212,260 (2016).

45. Oh, J.H., An, S.I., Shin, J. & Kug, J.S. Centennial memory of the Arctic Ocean for future Arctic climate recovery in response to a carbon dioxide removal. *Earth's Future* **10**, e2022EF002804 (2022).

46. Bronselaer, B., Zanna, L. Heat and carbon coupling reveals ocean warming due to circulation changes. *Nature* **584,** 227–233 (2020).

47. Matsumura, S., Ueki, S. & Horinouchi, T. Contrasting responses of midlatitude jets to the North Pacific and North Atlantic warming. *Geophysical research letters* **46**, 3973-3981 (2019).

48. Yeh, S.W. *et al.* ENSO atmospheric teleconnections and their response to greenhouse gas forcing. *Reviews of Geophysics* **56**, 185-206 (2018).

49. Shaw, T.A., Barpanda, P. & Donohoe, A. A moist static energy framework for zonal-mean storm-track intensity. *Journal of the Atmospheric Sciences* **75**, 1979-1994 (2018).

50. Chemke, R. The future poleward shift of Southern Hemisphere summer mid-latitude storm tracks stems from ocean coupling. *Nature communications* **13**, 1730 (2022).

51. Ayres, H. & Screen, J. Multimodel analysis of the atmospheric response to Antarctic sea ice loss at quadrupled CO2. *Geophysical Research Letters* **46**, 9861-9869 (2019).

52. Screen, J.A., Eade, R., Smith, D.M., Thomson, S. & Yu, H. Net equatorward shift of the jet streams when the contribution from sea-ice loss is constrained by observed eddy feedback. *Geophysical Research Letters* **49**, e2022GL100523 (2022).

53. Lyu, K., Zhang, X., Church, J.A. & Wu, Q. Processes responsible for the Southern Hemisphere ocean heat uptake and redistribution under anthropogenic warming. *Journal of Climate* **33**, 3787-3807 (2020).

54. Liu, W., Lu, J., Xie, S.-P. & Fedorov, A. Southern Ocean heat uptake, redistribution, and storage in a warming climate: The role of meridional overturning circulation. *Journal of Climate* **31**, 4727-4743 (2018).

55. Held, I.M. *et al.* Probing the fast and slow components of global warming by returning abruptly to preindustrial forcing. *Journal of Climate* **23**, 2418-2427 (2010).

56. Long, S.-M., Xie, S.-P., Zheng, X.-T. & Liu, Q. Fast and slow responses to global warming: Sea surface temperature and precipitation patterns. *Journal of Climate* **27**, 285-299 (2014).

57. Schleussner, C.-F. *et al.* Differential climate impacts for policy-relevant limits to global warming: the case of 1.5 C and 2 C. *Earth system dynamics* **7**, 327-351 (2016).

58. Tebaldi, C., Armbruster, A., Engler, H. & Link, R. Emulating climate extreme indices. *Environmental Research Letters* **15**, 074006 (2020).

59. Gertler, C.G. *et al.* Weakening of the extratropical storm tracks in solar geoengineering scenarios. *Geophysical Research Letters* **47**, e2020GL087348 (2020).

60. Pinto, J.G., Fröhlich, E., Leckebusch, G. & Ulbrich, U. Changing European storm loss potentials under modified climate conditions according to ensemble simulations of the ECHAM5/MPI-OM1 GCM. *Natural Hazards and Earth System Sciences* **7**, 165-175 (2007).

61. Schwierz, C. *et al.* Modelling European winter wind storm losses in current and future climate. *Climatic change* **101**, 485-514 (2010).

Methods

Model & experimental design

To assess storm track response to a changing CO_2 pathway, an idealized ramp-up and -down experiment is conducted with Community Earth System Model (CESM)[62] version 1.2.2. This model is integrated with a horizontal resolution of 0.9º by 1.25º in the atmosphere and of 1º by 0.5º in the ocean (i.e., f09_g16 resolution). A total of 30 and 60 vertical levels are set for the atmosphere and ocean, respectively. The model output is archived at a spatial resolution of 2.5 º by 2.5 º except when calculating the latitudinal change of the storm track when the native model resolution is used instead. To test the robustness of the result, eight models of CMIP6 CDRMIP experiments are analyzed[18]. In addition, 20 models of CMIP6 historical and the shared socioeconomic pathways 585 scenarios, as well as 13 models of CMIP6 piControl and 1pctCO2 simulations are further examined[19].

The model experiment is composed of the following three stages: 1) ramp-up, 2) ramp-down, and 3) stabilization (Fig. 1a). As a reference, the present-day (PD) simulation is also conducted for 900 years, with CO_2 concentrations fixed to the values of the year 2000 (367 ppm). A total of 28 ensemble simulations are conducted with varying initial conditions. Each initial condition is chosen by considering interdecadal variability of SST. The 12 initial conditions are selected from six positive and six negative phases of Atlantic Multi-Decadal Variability[63] in the PD simulation. Similarly, 16 ensembles are chosen from eight positive and eight negative phases of Pacific Decadal Oscillation[64]. Starting from each initial condition, CO_2 concentrations are increased at the rate of 1% per year for 140 years until quadrupled (2001-2140: RU). They are then decreased at a same rate for 140 years (2141-2280: RD), similar to CDRMIP protocol. The CO_2 concentrations are then maintained at the PD level for an additional 120 years in the stabilization period (2281-2400). In this study, consecutive 300 years of the PD simulation, within which 28 initial states are selected, are utilized for the analysis.

Storm track

The storm track is defined by vertically-averaged eddy kinetic energy (EKE) with mass weighting[9,33,65,66]. The variables at three pressure levels (i.e., 200, 500, and 850 hPa) are utilized due to data availability. The three pressure levels are utilized to represent the three layers of 1000-675 hPa, 675-350 hPa, and 350-0 hPa. To isolate synoptic variability, a 2-8 day bandpass-filter is first applied to zonal and meridional winds. The three storm regions, centered on maximum hysteresis response regions (Fig. 2e), are specified for the regional analysis. They are the North Atlantic (NA; 40ºW-80ºE, 40º-60ºN), North Pacific (NP; 150º-230ºE, 30º-50ºN), and Southern Hemisphere (SH; 35°-60°S) regions. Although not shown, the overall results are not very sensitive to small shifts in the latitude of analysis domains. Other storm track definitions, such as the variance of 24-hour filtered meridional wind at 200 hPa[8] and the standard deviation of bandpass filtered geopotential height at 500 hPa[67], are also utilized to test the robustness of the results (Supplementary Fig. 3).

Lagrangian cyclone tracking

Individual cyclones are tracked by using 6-hourly relative vorticity at 850 hPa[68]. Specifically, extratropical cyclones are defined when the T42-filtered 850-hPa relative vorticity satisfies cyclone criteria, such as amplitude ≥ 1 CVU (cyclonic vorticity unit, 10^{-5} s^{-1} in the NH; -10^{-5} s^{-1} in the SH), lifetime ≥ 48 hours, travel distance ≥ 1000 km, and genesis at latitudes 20 degrees poleward in each hemisphere[32]. Cyclone density statistics are then calculated by considering an effective radius of 555 km[69]. The intense cyclones are also separately defined as those with a maximum vorticity exceeding the 90th percentile in each hemisphere for each month from the PD simulation[11].

505 **Mean available potential energy.**

506 The mean available potential energy[65,66,70] in midlatitudes is calculated as below:

507 $$MAPE = \frac{c_p}{2g}\int_{1000\ \mathrm{hPa}}^{200\ \mathrm{hPa}} \Gamma\left(\bar{T}^2 - \tilde{T}^2\right) dp \qquad (1)$$

508 where, Γ represents an inverse static stability ($\frac{-\kappa\theta}{pT}\left(\frac{\partial\tilde{\theta}}{\partial p}\right)^{-1}$). Overbar and tilde denote zonal-average

509 and area-weighted average in midlatitudes (30º-60º), respectively.

510

511 **Surface wind extreme**

512 Surface wind extreme is defined as a daily mean wind speed exceeding 98th percentile[71,72] for

513 each month from the PD simulation. The cyclone-related surface wind extreme is then defined as a

514 day when the cyclone passes over land[72]. Although a daily maximum wind speed or 6-hourly wind

515 speed is more commonly used to define wind extreme[71,72], a daily mean wind speed is utilized in this

516 study[73] due to data availability.

517

518 **Data availability**

519 The Data used in this study are available at https://doi.org/10.6084/m9.figshare.25239559 (ref. 74),

520 and the CMIP6 archives are freely available from https://esgf-node.llnl.gov/projects/cmip6.

521

522 **Code availability**

523 The analysis were carried out using the function in NCAR Command Language v.6.2.1 and Python

524 packages (scikit-learn 0.23.2). To carry out the interpolation of the model grid data, we utilized climate

525 data operators available at https://code.mpimet.mpg.de/projects/cdo. All figures are generated using

526 the Grid Analysis and Display System (GrADS) v.2.2.1 (http://cola.gmu.edu/grads), and the codes are

527 available at https://doi.org/10.6084/m9.figshare.25239559 (ref. 74).

Methods-only references

62. Hurrell, J.W. *et al.* The community earth system model: a framework for collaborative research. *Bulletin of the American Meteorological Society* **94**, 1339-1360 (2013).

63. Trenberth, K.E. & Shea, D.J. Atlantic hurricanes and natural variability in 2005. *Geophysical research letters* **33** (2006).

64. Mantua, N.J., Hare, S.R., Zhang, Y., Wallace, J.M. & Francis, R.C. A Pacific interdecadal climate oscillation with impacts on salmon production. *Bulletin of the american Meteorological Society* **78**, 1069-1080 (1997).

65. Chemke, R., Ming, Y. & Yuval, J. The intensification of winter mid-latitude storm tracks in the Southern Hemisphere. *Nature climate change* **12**, 553-557 (2022).

66. O'Gorman, P.A. Understanding the varied response of the extratropical storm tracks to climate change. *Proceedings of the National Academy of Sciences* **107**, 19176-19180 (2010).

67. Blackmon, M.L. A climatological spectral study of the 500 mb geopotential height of the Northern Hemisphere. *Journal of the Atmospheric Sciences* **33**, 1607-1623 (1976).

68. Hoskins, B.J. & Hodges, K.I. New perspectives on the Northern Hemisphere winter storm tracks. *Journal of the Atmospheric Sciences* **59**, 1041-1061 (2002).

69. Lee, J. *et al.* Extratropical cyclones over East Asia: Climatology, seasonal cycle, and long-term trend. *Climate Dynamics* **54**, 1131-1144 (2020).

70. Peixoto, J.P., Oort, A.H. & Lorenz, E.N. *Physics of climate*, Vol. 520. (Springer, 1992).

71. Klawa, M. & Ulbrich, U. A model for the estimation of storm losses and the identification of severe winter storms in Germany. *Natural Hazards and Earth System Sciences* **3**, 725-732 (2003).

72. Little, A.S., Priestley, M.D. & Catto, J.L. Future increased risk from extratropical windstorms in northern Europe. *Nature Communications* **14**, 4434 (2023).

73. Rockel, B. & Woth, K. Extremes of near-surface wind speed over Europe and their future changes as estimated from an ensemble of RCM simulations. *Climatic Change* **81**, 267-280 (2007).

74. Hwang, J. Data and codes for "Asymmetric hysteresis response of midlatitude storm tracks to CO_2 removal". https://doi.org/10.6084/m9.figshare.25239559 (2024).

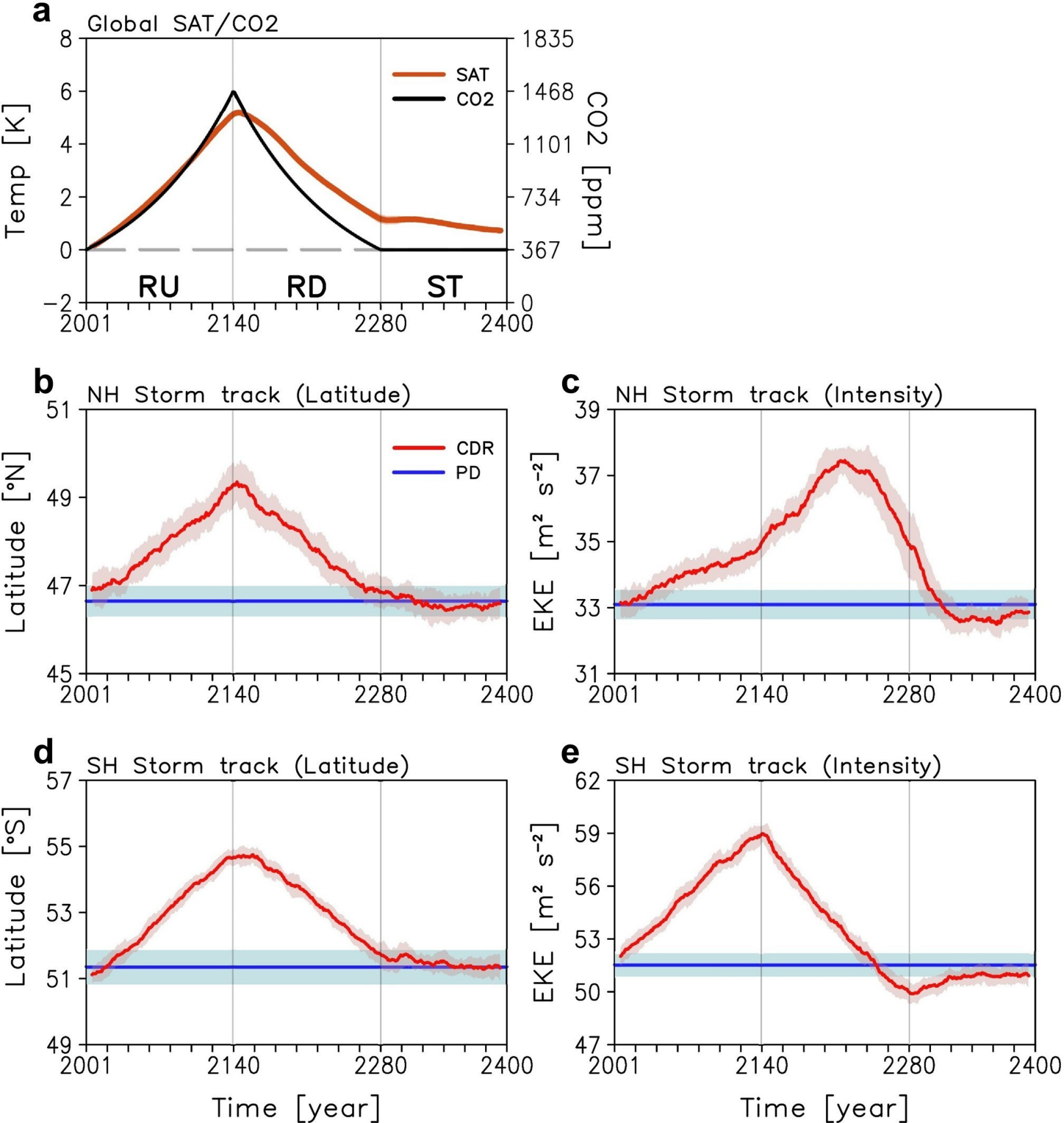
a
Global SAT/CO2
Temp [K]
CO2 [ppm]
SAT
CO2
RU
RD
ST
2001
2140
2280
2400
b
NH Storm track (Latitude)
Latitude [°N]
CDR
PD
c
NH Storm track (Intensity)
EKE [m² s⁻²]
d
SH Storm track (Latitude)
Latitude [°S]
e
SH Storm track (Intensity)
EKE [m² s⁻²]
Time [year]
Time [year]

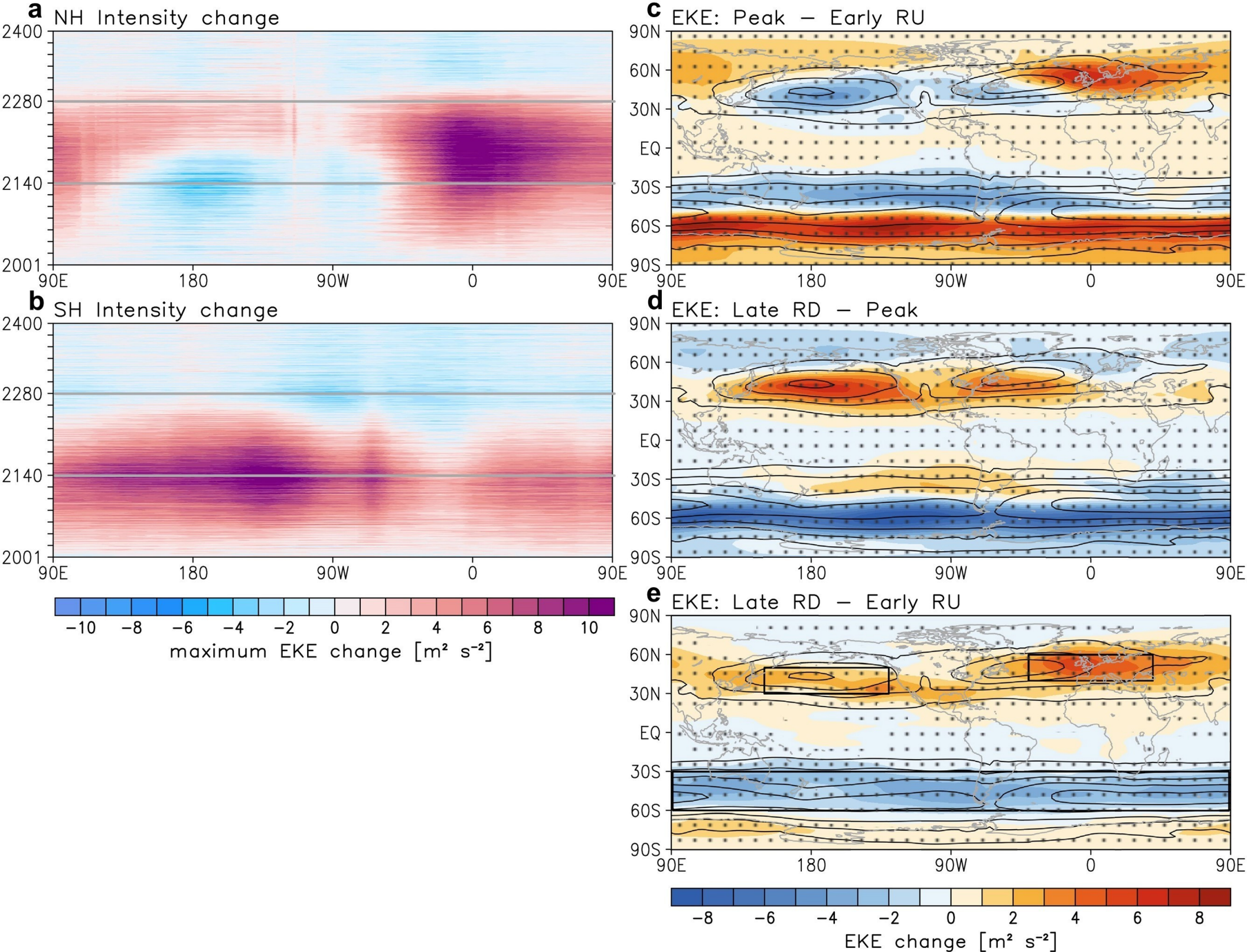
a
NH Intensity change
2400
2280
2140
2001
90E
180
90W
0
90E
b
SH Intensity change
2400
2280
2140
2001
90E
180
90W
0
90E
−10
−8
−6
−4
−2
0
2
4
6
8
10
maximum EKE change [m² s⁻²]
c
EKE: Peak − Early RU
90N
60N
30N
EQ
30S
60S
90S
90E
180
90W
0
90E
d
EKE: Late RD − Peak
90N
60N
30N
EQ
30S
60S
90S
90E
180
90W
0
90E
e
EKE: Late RD − Early RU
90N
60N
30N
EQ
30S
60S
90S
90E
180
90W
0
90E
−8
−6
−4
−2
0
2
4
6
8
EKE change [m² s⁻²]

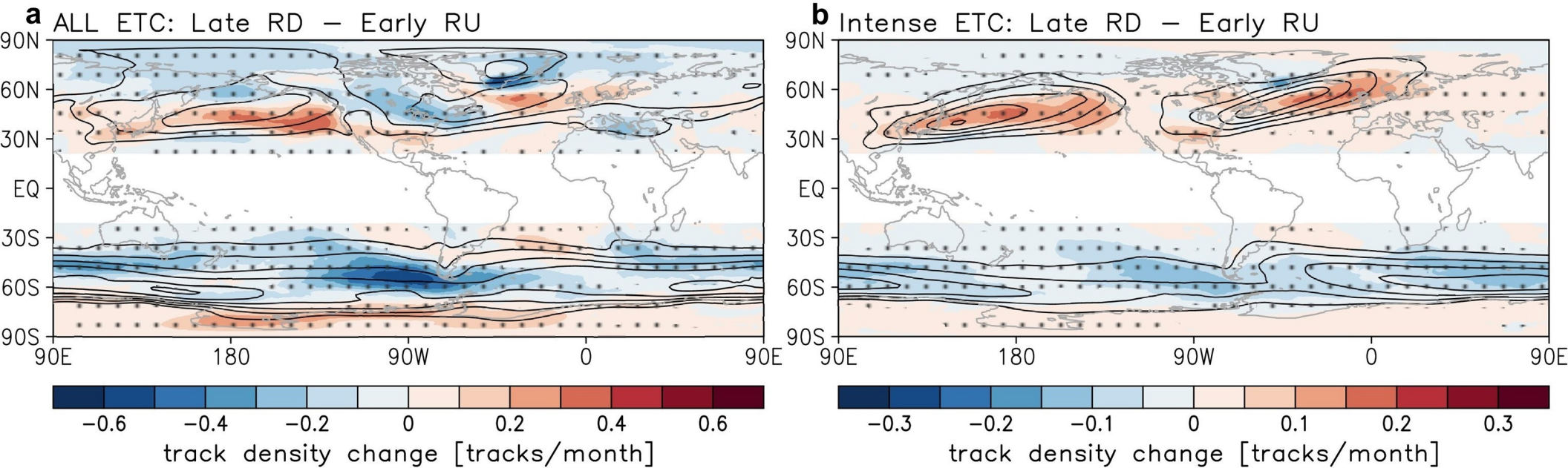
a
ALL ETC: Late RD − Early RU
90N
60N
30N
EQ
30S
60S
90S
90E
180
90W
0
90E
−0.6
−0.4
−0.2
0
0.2
0.4
0.6
track density change [tracks/month]
b
Intense ETC: Late RD − Early RU
90N
60N
30N
EQ
30S
60S
90S
90E
180
90W
0
90E
−0.3
−0.2
−0.1
0
0.1
0.2
0.3
track density change [tracks/month]

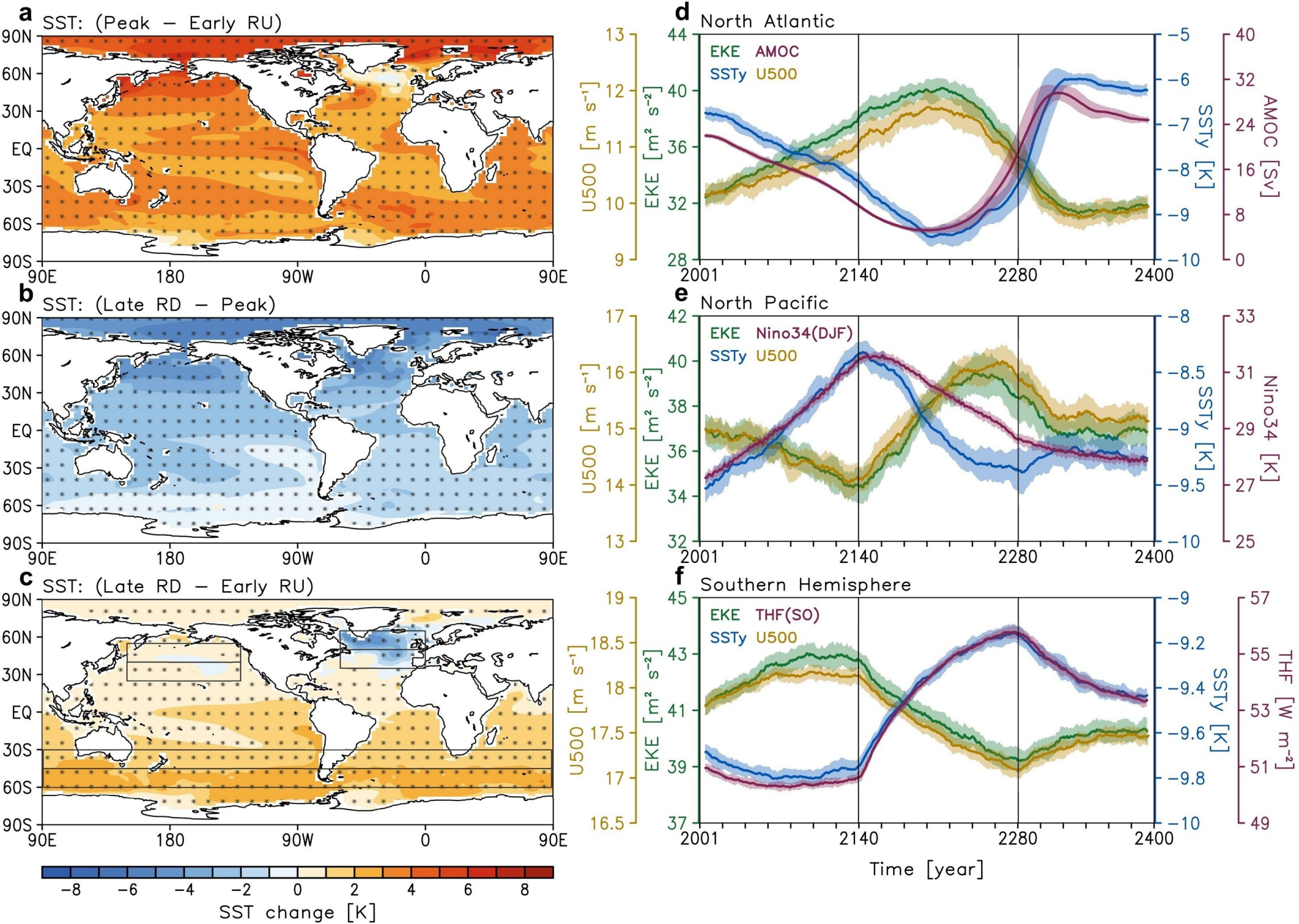
a
SST: (Peak − Early RU)
b
SST: (Late RD − Peak)
c
SST: (Late RD − Early RU)
90N
60N
30N
EQ
30S
60S
90S
90E
180
90W
0
−8
−6
−4
−2
0
2
4
6
8
SST change [K]
d
North Atlantic
EKE
AMOC
SSTy
U500
U500 [m s⁻¹]
EKE [m² s⁻²]
SSTy [K]
AMOC [Sv]
e
North Pacific
Nino34(DJF)
Nino34 [K]
f
Southern Hemisphere
THF(SO)
THF [W m⁻²]
2001
2140
2280
2400
Time [year]

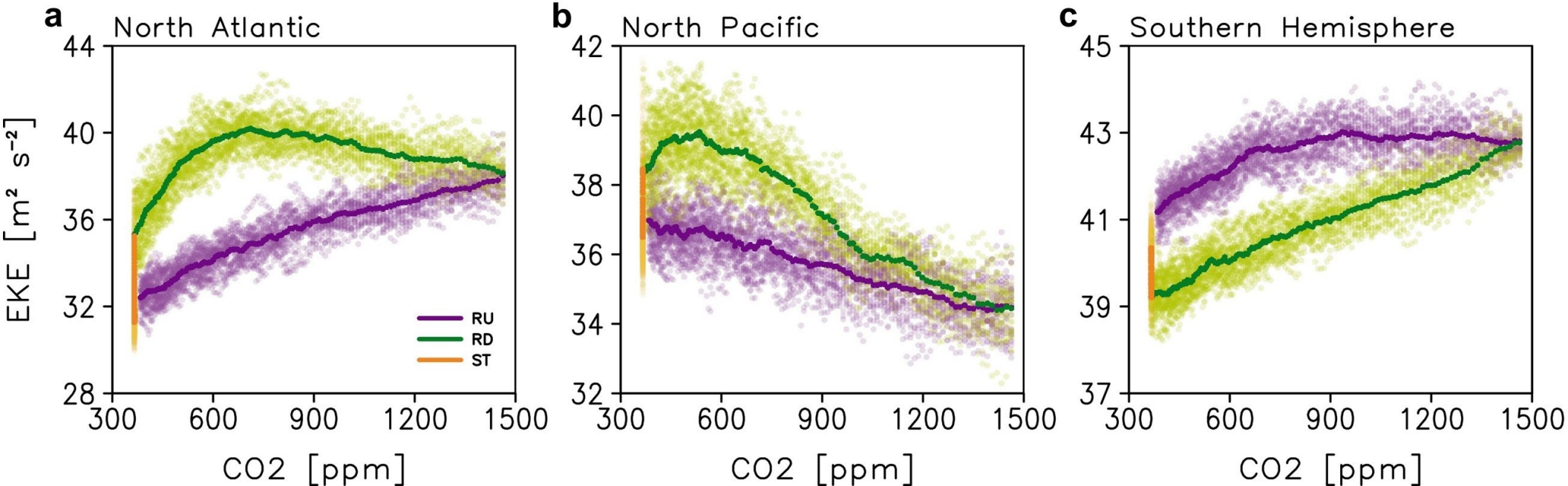
a
North Atlantic
b
North Pacific
c
Southern Hemisphere
EKE [m² s⁻²]
CO2 [ppm]
RU
RD
ST
44
40
36
32
28
42
38
34
45
43
41
39
37
300
600
900
1200
1500